

An Efficient Method for Generating Equilibrium Phase Diagrams of Isostructural and Heterostructural Two-Dimensional Alloys from First Principles

John Cavin^{1,*} and Rohan Mishra^{2,†}

¹Department of Physics, Washington University in St. Louis, St. Louis, MO 63130, USA.

²Department of Mechanical Engineering and Material Science, and Institute of Materials Science and Engineering, Washington University in St. Louis, St. Louis, MO 63130, USA.

Abstract

Alloying is a successful strategy for tuning the phases and properties of two-dimensional (2D) transition metal dichalcogenides (TMDCs). To accelerate the synthesis of new TMDC alloys, we present a method for generating temperature-composition equilibrium phase diagrams by combining first-principles total energy calculations with thermodynamic solution models. This method is applied to three representative 2D TMDC alloys: an isostructural alloy, $\text{MoS}_{2(1-x)}\text{Te}_{2x}$, and two heterostructural alloys, $\text{Mo}_{1-x}\text{W}_x\text{Te}_2$ and $\text{WS}_{2(1-x)}\text{Te}_{2x}$. We show that the mixing enthalpy of the entire composition range of these binary alloys can be reliably represented using a sub-regular solution model fitted to the total energy of a small number of compositions — that are calculated using density-functional theory on special quasi-random structures. The sub-regular solution model uses a cubic fit that captures three-body effects that are important in these TMDC alloys having hexagonal structures. By comparing both isostructural and heterostructural phase

*Corresponding author: john.cavin@northwestern.edu

†Corresponding author: rmishra@wustl.edu

diagrams generated with this method to those calculated with cluster expansion methods, we demonstrate that this method can be used to rapidly design phase diagrams of TMDC alloys, and related 2D materials.

Introduction

Monolayer transition metal dichalcogenides (TMDCs) form a large class of two-dimensional (2D) materials displaying a diverse array of properties, including direct band gaps [1], superconductivity [2], topological insulation [3], spin and valley polarization [4-6], and charge density waves [7,8]. TMDCs have a stoichiometry of MX_2 , where M is a transition metal and X is a chalcogen (S, Se, and Te). The combinatorics of the available transition metal and chalcogen choices, and the variety of crystal structures TMDCs can adapt are responsible for their diverse properties. Consequently, alloying two or more transition metals or chalcogens has been a successful method for improving their performance in electronics [9,10] and optoelectronics [11-13], and as catalysts for a variety of reactions including hydrogen evolution [14], carbon dioxide reduction [15,16], and oxygen evolution and reduction [15]. Not only the properties, but the alloy structure or phase is also sensitive to composition. Common polytypes of monolayer TMDCs include the $2H$ phase where the transition metal is in a trigonal prismatic coordination of the chalcogen atoms, the $1T$ phase where the transition metal in an octahedral coordination, and $1T'$ phase with the metal atoms in a distorted octahedral coordination. For a given composition, different polytypes can have vastly different properties. For example, monolayer MoS_2 in the $2H$ phase is a direct band gap semiconductor with a lack of inversion symmetry that imparts a valley degree of freedom [17]; its $1T$ phase is metallic, which makes it attractive for electrocatalysis [18]; and its $1T'$ phase is a topological insulator protected by inversion symmetry [3]. By alloying two

TMDCs with different ground state polytypes, a process referred to as heterostructural alloying, it is possible to stabilize an otherwise metastable polytype, and obtain new functionalities [19]. This method of phase engineering through heterostructural alloys has been used to stabilize the $2H$ and $1T'$ phases in $WSe_{2(1-x)}Te_{2x}$ [12].

For isostructural and heterostructural alloys alike, identifying regions in the temperature-composition space where a single phase of the alloy is stable can accelerate their synthesis. This relationship is summarized quantitatively through equilibrium temperature-composition phase diagrams. Isostructural alloys typically have the same crystal structure as their end members, although there are exceptions [20]. Hence, their phase diagrams are relatively straight forward and provide a miscibility temperature above which the alloy is stable in a single phase. Such phase diagrams can be generated from thermodynamic quantities obtained using first-principles density-functional-theory (DFT) calculations [20-22]. Isostructural alloys of monolayer TMDCs have received widespread attention following reports of their theoretical phase diagrams. Kang et al. reported one of the first phase diagrams of 2D chalcogen alloys of group VI transition metals having the $2H$ phase [23,24]. A recent work reported the experimental realization of several isostructural TMDC alloys involving group V and VI transition metals, with alloying at both the metal- and chalcogen-sites, using theoretically predicted phase diagrams [15]. In contrast to isostructural alloys, heterostructural TMDC alloys — where the end members have different crystal structure — are starting to garner attention only recently [25-30]. The phase diagrams of heterostructural alloys are comparatively nontrivial, having multiple phase boundaries. There are only a handful of examples of phase diagrams of heterostructural 2D TMDC alloys; many of them have been obtained using time-consuming growth experiments at different temperatures and compositions followed by characterization [25,30]. Relatively few diagrams have been predicted

theoretically, such as the report on $\text{Mo}_{1-x}\text{W}_x\text{Te}_2$, a heterostructural alloy of $2H$ MoTe_2 and $1T'$ WTe_2 , by Duerloo et al. [31].

In this Letter, we present an efficient framework to generate equilibrium phase diagrams of 2D TMDC alloys that are based on a limited number of DFT calculations. We fit the mixing enthalpy of the alloys with a cubic sub-regular solution model that can capture the important interactions between the triplet clusters in TMDCs. We apply this method to generate the phase diagrams of heterostructural TMDC alloys $\text{Mo}_{1-x}\text{W}_x\text{Te}_2$ and $\text{WS}_{2(1-x)}\text{Te}_{2x}$, and the isostructural alloy $\text{MoS}_{2(1-x)}\text{Te}_{2x}$, for contrast. The phase diagram of $\text{Mo}_{1-x}\text{W}_x\text{Te}_2$ is found to closely match the one derived using time-consuming cluster expansion models [31]. Similarly, the phase diagram of the isostructural alloy $\text{MoS}_{2(1-x)}\text{Te}_{2x}$ shows good agreement with that generated by Kang et al using cluster expansion models [23,24]. The phase diagram of $\text{Mo}_{1-x}\text{W}_x\text{Te}_2$ has a large region of metastability with no unstable region and a cross-over from $2H$ to $1T'$ ground state at $x \sim 0.33$, making it a good candidate for phase engineering. In contrast, $\text{WS}_{2(1-x)}\text{Te}_{2x}$ has a large region where the alloys are unstable and are expected to segregate, and a cross-over from $2H$ to $1T'$ phase at $x = 0.9$. This indicates that the $1T'$ phase is difficult to stabilize in WS_2 , but a large concentration of Te can be added to WS_2 , while maintaining the semiconducting $2H$ phase. This method can be rapidly applied to the large space of TMDC alloys with various polytypes, and other related 2D materials such as MXenes.

Methodology

A standard method for generating equilibrium phase diagrams is by using semi-grand canonical ensemble lattice Monte Carlo simulations to determine phase boundaries directly

through thermodynamic integration [32]. These Monte Carlo simulations are typically carried out through the cluster expansion method [33,34]. Cluster expansions decompose the internal energy of an alloy into a sum over cluster contributions. This method is useful if the sum converges quickly with respect to the maximum cluster size included. By performing *ab initio* DFT calculations on many relatively small supercells with varying alloy configurations, the energy of 1-, 2-, and 3-body clusters can be fit with least squares regression. These simulations can individually be quite expensive and cumulatively are even more so as many are required to perform the thermodynamic integration.

A more straightforward method to generate phase diagrams is to use the common tangent construction and metastability analysis on analytical expressions of the Gibbs free energies of all the relevant alloy phases. Specifically, the free energy of mixing of the alloy with respect to its end members, ΔG_{mix} , is required for all intermediate compositions, $x \in (0,1)$. The Gibbs free energy is composed of two terms:

$$\Delta G_{\text{mix}} = \Delta H_{\text{mix}} - T \Delta S_{\text{mix}}, \quad (1)$$

where ΔH_{mix} and ΔS_{mix} are the enthalpy and the entropy of mixing, respectively, and T is the temperature. The mixing entropy, ΔS_{mix} , can be approximated with the configurational entropy:

$$\Delta S = -k_B [x \ln x + (1 - x) \ln(1 - x)]. \quad (2)$$

Here, k_B is the Boltzmann constant. One method to get an analytical form for ΔH_{mix} is to use a cluster expansion as outlined before. Replacing the correlation functions present in a cluster expansion sum with the statistical values in a random alloy gives a polynomial expression for ΔH_{mix} . The degree of the polynomial directly corresponds to the largest cluster size included in

the expansion where using up to N -element clusters corresponds to a N^{th} degree polynomial. This procedure has been used before for constructing phase diagrams of binary TMDC alloys [23,31].

An alternative method to get an expression for mixing enthalpy is to directly perform a polynomial fit — that emulates a thermodynamic solution model — to calculated enthalpies at various compositions. A brute force approach is to create large supercells with pseudorandom occupation of sites corresponding to many composition values and fitting the results to a polynomial as has been applied for bulk semiconductor alloys [35]. A more convenient method is to use special quasirandom structures (SQS's) [36,37], which are relatively small supercells having site occupations that closely mimic the distribution of clusters found in a random alloy with the same composition. This means that properties that can be expressed as a sum of small clusters will be accurately calculated from the SQS. Because enthalpy expressions can be determined with a relatively small number of moderately-sized SQS's, we chose this method. The generation of SQS's was facilitated by a reverse monte Carlo method implemented in the Alloy Theoretic Automated Toolkit (ATAT) [34]. Because SQS's suitably mimic the clusters of a theoretical alloy, only one calculation is required per composition value, and because they are significantly smaller than pseudorandomly occupied supercells required for similar accuracy, they are advantageous in terms of computation time [37,38]. These considerations make SQS's a powerful tool for scalable generation of equilibrium phase diagrams.

With an expression for the free energy, the composition space can be divided into different regions of stability for a fixed temperature. This procedure is repeated over a grid of temperatures to fully develop the phase boundaries and determine the full equilibrium phase diagram. For an isostructural alloy, there can be three regions: stable, metastable, and unstable. The stable region is the set of compositions where the single-phase alloy is on the convex hull. Outside of this region,

metastability is determined by the curvature of the free energy, i.e., $\frac{d^2}{dx^2} \Delta G_{\text{mix}}$. When the curvature is positive and the free energy itself is not on the convex hull, the free energy of the alloy is lower than the average energy of two infinitesimally close compositions on the adjacent side of the alloy. Therefore, in this region, the single-phase alloy is metastable in the sense that it is stable to small fluctuations. However, if the curvature of the free energy is negative, infinitesimal phase decompositions *lower* the free energy compared to the single-phase alloy. Therefore, the metastable and unstable regions correspond to positive and negative curvatures of the free energy, respectively, outside the convex hull. The binodal boundary between these regions is demarked by an inflection point. This treatment is easily generalized to multiple structural phases by including multiple free energy surfaces in the convex hull analysis leading to different stable regions for each morphology.

Computational Details

Disordered 2D alloys were studied using 6×6 and 3×6 supercells of the primitive cell of $2H$ -phase and $1T'$ -phase TMDCs, respectively. Slab models with vacuum along the out-of-plane direction were used to simulate 2D layers. To eliminate interaction between image 2D layers, a vacuum spacing of $>15 \text{ \AA}$ in the out-of-plane direction was used. Total energies were calculated using DFT as implemented in the Vienna Ab-initio Simulation Package (VASP) using the Perdew-Burke-Ernzerhof exchange-correlation functional [39,40]. For the SQS's, geometric relaxation was conducted at only the Γ -point in reciprocal space. A subsequent static calculation for the electronic structure was performed using a Γ -centered $3 \times 3 \times 1$ k -points mesh generated using the Monkhorst-Pack method [41]. Pure TMDCs were studied using a k -points grid of $8 \times 8 \times 1$

for geometry optimization and $24 \times 24 \times 1$ for static calculations. A kinetic energy cutoff of 450 eV was used for all the calculations.

Results and Discussion

A recent paper by Hemmat et al. used the common-tangent construction method to generate equilibrium phase diagrams for 25 TMDC isostructural alloys with the $2H$ phase [15]. In that work, chalcogens were restricted to S and Se because many tellurides have the $1T'$ phase as their ground state. Here, we expand the method to generate phase diagrams for heterostructural TMDC alloys. We started with an isostructural TMDC alloy having Te, $\text{MoS}_{2(1-x)}\text{Te}_{2x}$. While bulk MoTe_2 can exist in either a distorted octahedral $1T'$ phase or the triangular prismatic $2H$ phase, monolayer MoTe_2 prefers the $2H$ phase [42,43]; and so does 2D MoSe_2 . An equilibrium phase diagram of $\text{MoS}_{2(1-x)}\text{Te}_{2x}$ generated using the cluster expansion method shows that it exists in the $2H$ phase for all compositions, x [23]. We use this alloy as a benchmark to compare the phase diagram generated using a solution model fitted to the energy of disordered SQSs. The mixing enthalpy of $\text{MoS}_{2(1-x)}\text{Te}_{2x}$, calculated using SQS, is shown in FIG. 1a. Because the mixing enthalpy is positive, the alloy is not miscible; that is, entropy is required to obtain a stable alloy in a single-phase.

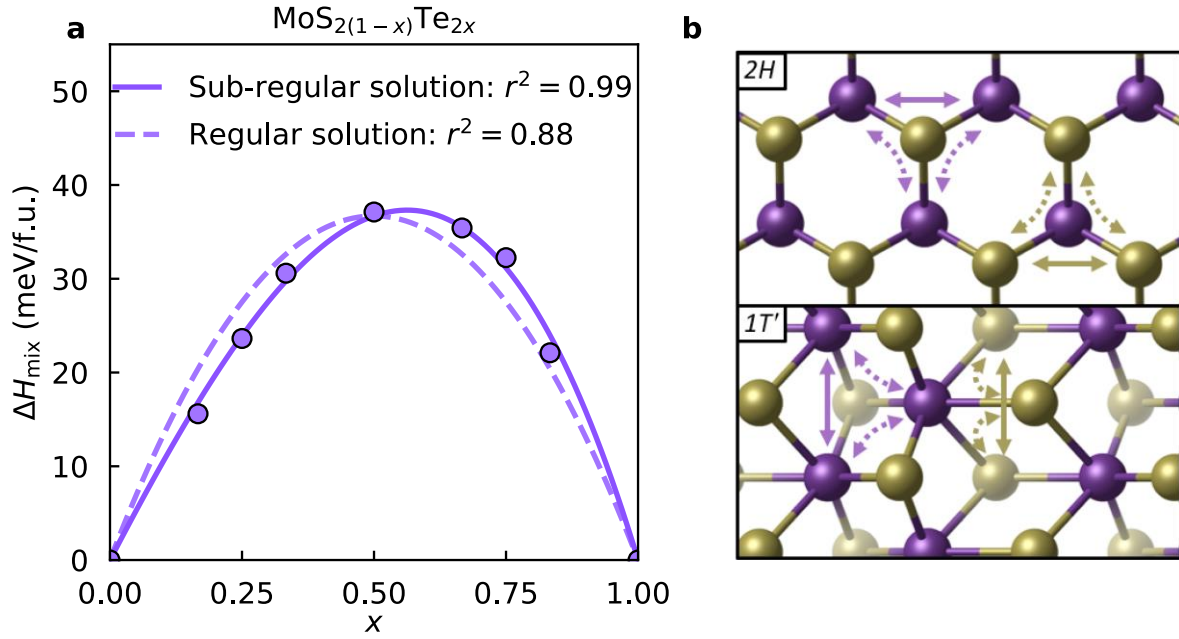


FIG. 1. Enthalpy of mixing of $\text{MoS}_{2(1-x)}\text{Te}_{2x}$ fitted to different solution models and atomic models justifying the need for a sub-regular solution model. (a) Mixing enthalpy from DFT calculation of SQS's at various compositions, shown as datapoints, with a quadratic regular solution model fit (dashed line) and cubic sub-regular solution model fit (solid line). (b) Visualizations of the $2H$ and $1T'$ phases showing how 3-body clusters are essential in 2D TMDCs. Transition metals are shown in purple and chalcogen atoms are shown in gold. Solid arrows indicate direct interactions between two sites, while dashed arrows indicate indirect interactions through a third site.

While the enthalpy of some alloys and solutions can be modeled as a regular solution with a quadratic fit, the asymmetry of the enthalpy in FIG. 1a clearly precludes this option. The regular solution model can be represented mathematically by the following equation:

$$\Delta H_{\text{mix}} = \Omega x(1 - x). \quad (3)$$

Assuming nearest neighbor interactions, the fitting parameter, Ω , represents the relative bonding strength between generic alloyed elements A and B in $A_{1-x}B_x$ compared to the $A-A$ and $B-B$ bonds. This can be expressed as:

$$\Omega = n \left(U_{AB} - \frac{1}{2} U_{AA} - \frac{1}{2} U_{BB} \right), \quad (4)$$

where n is the coordination number and the U 's are bonding energy contributions to the enthalpy. See Supplemental Materials for the derivation of Eq. (4) [44]. The regular solution model for this system is illustrated in FIG. 1a with a dashed line, which shows a poor fit. To capture the asymmetry of the enthalpy with respect to composition, a cubic sub-regular solution model is used. Such a model has the following general form:

$$\Delta H_{\text{mix}} = [\Omega_1(1 - x) + \Omega_2 x] x(1 - x). \quad (5)$$

In this form, the cubic sub-regular solution model can be seen as an average of two regular solution models weighted by x . A skewing of the enthalpy maximum to the right, i.e., $x > 0.5$, corresponds to $\Omega_2 > \Omega_1$. Similar to Equation (4), the fitting parameters in (5), Ω_1 and Ω_2 , have a microscopic interpretation related to the relative cluster energies. For a triangular lattice, the fitting parameters are given by:

$$\Omega_1 = 6 \left(U_{AB} - \frac{1}{2} U_{AA} - \frac{1}{2} U_{BB} + U_{AAB} - \frac{2}{3} U_{AAA} - \frac{1}{3} U_{BBB} \right) \quad (6)$$

and

$$\Omega_2 = 6 \left(U_{AB} - \frac{1}{2} U_{AA} - \frac{1}{2} U_{BB} + U_{ABB} - \frac{1}{3} U_{AAA} - \frac{2}{3} U_{BBB} \right). \quad (7)$$

See the Supplemental Material for a detailed derivation [44].

Just as the terms of the form U_{XY} correspond to the bonding energy between species X and Y , terms of the forms U_{XYZ} correspond to a three-body contribution to the enthalpy that is supplementary to the three corresponding two-body terms. Equations (6) and (7) can be seen as corrections to the coefficient defined by Equation (4). The additional correction terms themselves take on a similar form to Equation (4), corresponding to a difference between an alloy energy term

and a weighted average of the pure elemental terms. Therefore, a skewing of the enthalpy maximum to the right will correspond to a greater relative energy contribution from $A-B-B$ triplets compared to $A-A-B$ triplets. An opposite skew will correspond to an opposite relationship between the triplet energies.

We postulate that the requirement for a cubic fit of the enthalpy of $\text{MoS}_{2(1-x)}\text{Te}_{2x}$ is a natural consequence of the coordination of the $2H$ phase. While the regular solution model is derived from 2-body energy contributions, cubic terms become important when 3-body interactions cannot be ignored. FIG. 1b demonstrates why 3-body interactions are naturally important in quasibinary alloying of the $2H$ and $1T'$ phases compared to strictly binary alloys. The solid arrows represent an interaction between two alloyed sites. In quasibinary TMDC alloys, either the TM site or the chalcogen site can be alloyed. In either case, the interaction is facilitated through an intermediate chalcogen pair or transition metal, respectively. Connected to this intermediate is another TM or chalcogen — that we refer to as the tertiary site. The occupation of this tertiary site will affect the bonding properties of the intermediate site, making 2-body interactions insufficient as visualized by the dashed arrows. In the case of $1T'$ phase, there are many types of nearest neighbor 3-body clusters, but this does not change the argument for including a cubic term in the enthalpy. In the case of $\text{MoS}_{2(1-x)}\text{Te}_{2x}$, FIG. 1a shows the mixing enthalpy peak is shifted to the right, indicating that $\Omega_2 > \Omega_1$. From Equations (6) and (7), this asymmetry is determined to be caused by the relatively high energy of S-Te-Te clusters compared to S-S-Te clusters.

To show that fitting a sub-regular solution model to SQSs also works for heterostructural alloys, we applied it to the TM-site and chalcogen-site alloys $\text{Mo}_{1-x}\text{W}_x\text{Te}_2$ and $\text{WS}_{2(1-x)}\text{Te}_{2x}$, respectively. The steps for creating equilibrium phase diagrams for heterostructural alloys follow a very similar recipe of common tangent construction with the additional complication that free

energy curves must be determined for both endpoint phases. Furthermore, the appearance of the plotted mixing enthalpy takes on a qualitatively different form because it is calculated with respect to the ground state phase of the end points. FIG. 2a shows the calculated mixing enthalpy of $\text{Mo}_{1-x}\text{W}_x\text{Te}_2$ in the $2H$ and $1T'$ phases with cubic fits. The mixing enthalpies are positive, indicating that the alloy is immiscible, but the curvature is positive everywhere, indicating that a single-phase alloy is at worst metastable, i.e., it does not have any unstable region. In contrast, the mixing enthalpy of $\text{WS}_{2(1-x)}\text{Te}_{2x}$, shown in FIG. 2b, is seen to be comparatively high and has a negative curvature (concave down). This means that stabilization of a single phase will require a higher temperature and that there will be an unstable region where the alloy will be driven to phase segregation.

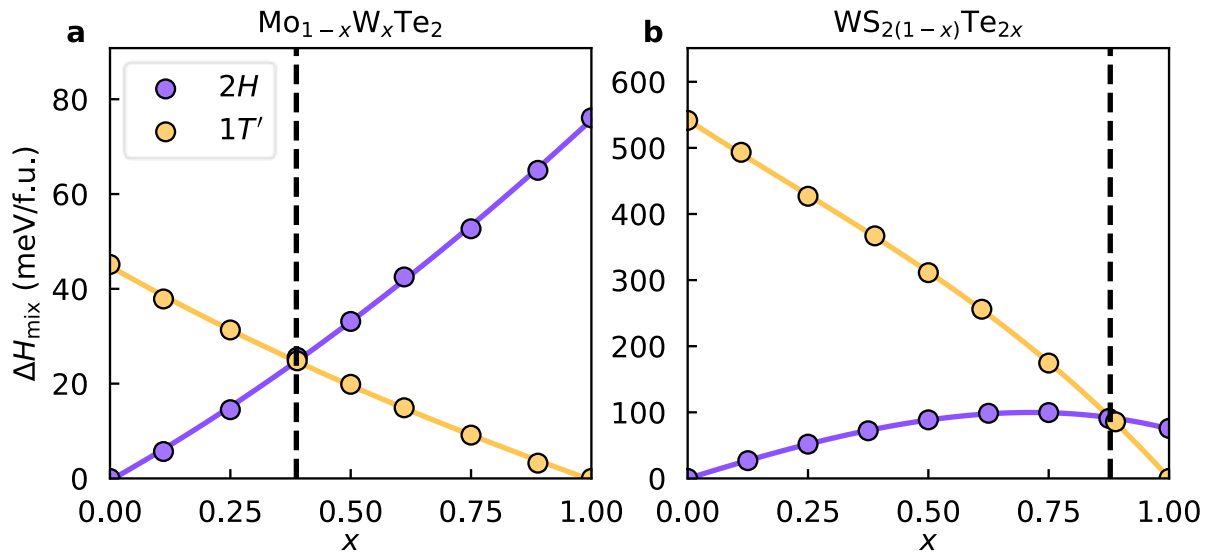


FIG. 2. Enthalpy of mixing for two heterostructural TMDC alloys with cubic sub-regular solution model fits. (a) $\text{Mo}_{1-x}\text{W}_x\text{Te}_2$, a TM-site heterostructural alloy. (b) $\text{WS}_{2(1-x)}\text{Te}_{2x}$, a chalcogen-site heterostructural alloy. The vertical dashed line denotes the composition where the stable phase changes.

With analytical expressions for the enthalpy of mixing for the isostructural and heterostructural alloys, we have half of the expression for the Gibbs free energy. The other half requires an analytical expression for the entropy of mixing. The entropy of an alloy is a sum of configurational entropy and other sources of entropy such as from vibrations. If we assume that these other contributions extrapolate linearly from the end-member materials, the configurational entropy is the primary contribution to ΔS_{mix} . Because configurational entropy has a simple functional form (Equation (1)), we have an expression for the free energy. FIG. 3a and FIG. 3b show the free energies of isostructural $\text{MoS}_{2(1-x)}\text{Te}_{2x}$ and heterostructural $\text{Mo}_{1-x}\text{W}_x\text{Te}_2$, respectively, at 400 K. Through the common tangent construction, the dashed lines show the free energy of a phase segregated alloy. In the case of $\text{MoS}_{2(1-x)}\text{Te}_{2x}$, this indicates segregation into an S-rich $2H$ phase and a Te-rich $2H$ phase. For $\text{Mo}_{1-x}\text{W}_x\text{Te}_2$, the dashed line indicates segregation into an Mo-rich $2H$ phase and a W-rich $1T'$ phase. In alloys where the curvature of the free energy is negative, this region is further divided into a metastable and an unstable region corresponding to positive and negative curvature of the free energy, respectively. This boundary is demarked in FIG. 3a with vertical dashes at the inflection points. Because the curvature of the mixing enthalpy of $\text{Mo}_{1-x}\text{W}_x\text{Te}_2$ is negative (FIG. 2b), there is no inflection point in the free energy and no unstable region. Repeating this analysis of the free energy over a grid of temperature values gives boundaries dividing the different regions of stability which define the equilibrium phase diagram.

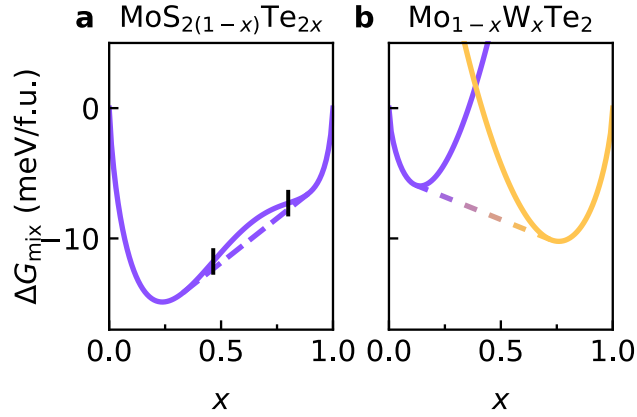


FIG. 3. Free energy of an isostructural and a heterostructural alloy at 400 K. (a) $\text{MoS}_{2(1-x)}\text{Te}_{2x}$, an isostructural alloy. Vertical black dashes indicate the boundary between the unstable and metastable regions (inflection points). (b) $\text{Mo}_{1-x}\text{W}_x\text{Te}_2$, a heterostructural alloy. The colored dash lines denote the free energy of a mixed phase.

The equilibrium phase diagrams for $\text{MoS}_{2(1-x)}\text{Te}_{2x}$, $\text{Mo}_{1-x}\text{W}_x\text{Te}_2$, and $\text{WS}_{2(1-x)}\text{Te}_{2x}$ are shown in FIG. 4. The equilibrium phase diagram for $\text{MoS}_{2(1-x)}\text{Te}_{2x}$ is shown in FIG. 4a. Because the alloy is isostructural, the phase diagram is relatively straightforward with a single stable region and a single unstable region with two metastable regions connected at the critical point. The temperature at the critical point is known as the miscibility temperature, the temperature above which the alloy is stable at all compositions. We note that the slight asymmetry of the enthalpy in FIG. 1a led to more substantial asymmetry in the phase diagram, making Te-rich alloys more difficult to synthesize in a single phase. The predicted asymmetries in the phase diagram of some $2H$ TMDC alloys was experimentally verified in a previous work [15]. This phase diagram generated with the SQS method is nearly identical in miscibility temperature and asymmetry to previous cluster expansion-based works where the metastable region was omitted [23,24].

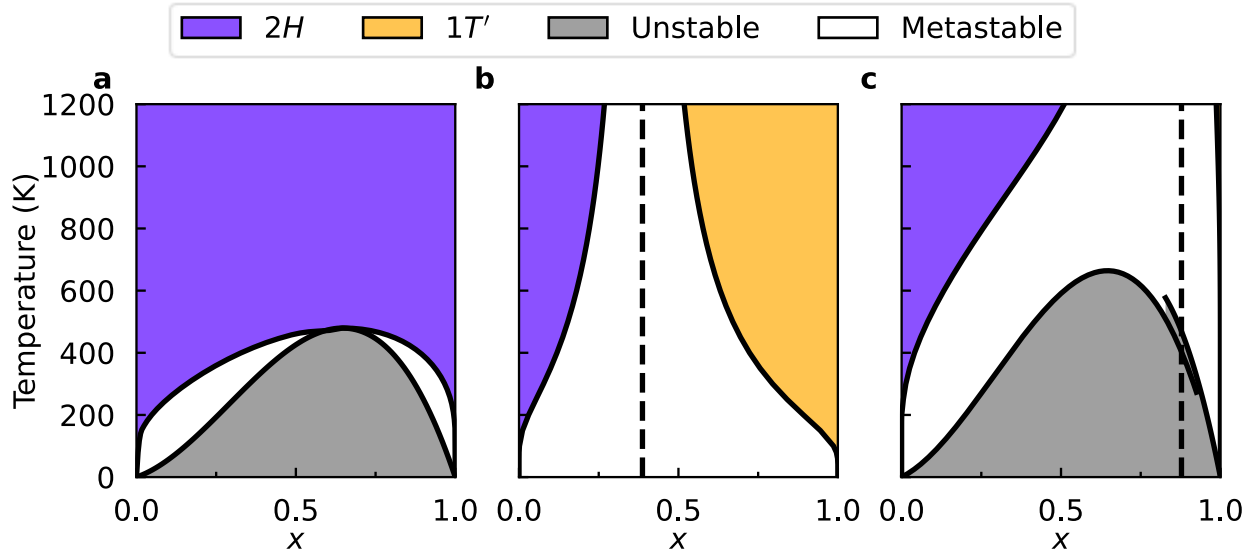


FIG. 4. Equilibrium phase diagrams for three representative TMDC alloys. (a) $\text{MoS}_{2(1-x)}\text{Te}_{2x}$, an isostructural alloy. (b) $\text{Mo}_{1-x}\text{W}_x\text{Te}_2$, a heterostructural alloy without an unstable region. (c) $\text{WS}_{2(1-x)}\text{Te}_{2x}$, a heterostructural alloy with an unstable region. Vertical dashed lines in (b) and (c) correspond to the composition where the stable phase changes.

The equilibrium phase diagram of $\text{Mo}_{1-x}\text{W}_x\text{Te}_2$ shown in FIG. 4b is more complicated because of its heterostructural nature. One simplification is that there is no unstable region due to the positive curvature of the mixing enthalpy (FIG. 2b) for all x . The large metastable region and the near-equimolar cross-over concentration makes this a promising material for phase engineering. These results are qualitatively similar to a work using cluster expansions, quadratic fits, and thermal expansion considerations [31].

Lastly, the phase diagram for $\text{WS}_{2(1-x)}\text{Te}_{2x}$ is shown in FIG. 4c. This heterostructural alloy produces the most complex phase diagram of the three because of its unstable region. Because the curvature of the mixing enthalpies corresponding to the two phases are different, the unstable region is defined piecewise with an ambiguous crossover region. WS_2 strongly favors the 2H phase with the DFT-calculated difference in energy of 2H and 1T' phase, $\Delta E_{(1T' - 2H)} = 542$ meV/f.u. Therefore, the crossover region for the alloy is at a very high Te content, indicating that the 1T'

phase of the alloy is difficult to realize experimentally. This could possibly be overcome by using Se instead of S because WSe₂ is less energetically opposed to the $1T'$ phase with $\Delta E_{(1T' - 2H)} = 279$ meV/f.u.. While to our knowledge this is the first generation of a heterostructural phase diagram for WS_{2(1-x)}Te_{2x}, a phase diagram for this alloy assuming only the $2H$ phase shows agreement with our unstable region [23,24].

Conclusion

Recent work has shown that the generation of equilibrium phase diagrams can successfully lead to the discovery of new miscible 2D alloys and in guiding the synthesis of immiscible 2D alloys [15]. Furthermore, heterostructural 2D alloys have become a promising platform for tuning properties and phase engineering. We have presented a method for generating these phase diagrams that is standardized and only requires a few calculations of moderately sized SQS's. We showed that this method is applicable to both isostructural and heterostructural alloys and it produces results that agree with previous works using more computationally intensive methods. This method of generating equilibrium phase diagrams has the potential to accelerate the expanding field of 2D alloys by providing guidance for the synthesis of new 2D materials, such as high-entropy alloys of TMDCs and MXenes [16,45].

Acknowledgements

This work was supported by the National Science Foundation (NSF) through a DMREF grant CBET-1729787. This work used computational resources of the Extreme Science and Engineering Discovery Environment (XSEDE), which is supported by NSF ACI-1548562. The authors thank Dr. Sung Beom Cho for useful discussions.

References

- [1] A. Splendiani, L. Sun, Y. Zhang, T. Li, J. Kim, C.-Y. Chim, G. Galli, and F. Wang, *Nano Letters* **10**, 1271 (2010).
- [2] Y. Saito, T. Nojima, and Y. Iwasa, *Nature Reviews Materials* **2**, 16094 (2016).
- [3] X. Qian, J. Liu, L. Fu, and J. Li, *Science* **346**, 1344 (2014).
- [4] K. F. Mak, K. L. McGill, J. Park, and P. L. McEuen, *Science* **344**, 1489 (2014).
- [5] J. Zhou *et al.*, *Adv Mater* **32**, 1906536 (2020).
- [6] R. Mishra, W. Zhou, S. J. Pennycook, S. T. Pantelides, and J. C. Idrobo, *Physical Review B* **88**, 144409 (2013).
- [7] A. W. Tsen *et al.*, *Proc Natl Acad Sci U S A* **112**, 15054 (2015).
- [8] K. Rossnagel, *Journal of Physics: Condensed Matter* **23**, 213001 (2011).
- [9] X. Hu, Z. Hemmat, L. Majidi, J. Cavin, R. Mishra, A. Salehi-Khojin, S. Ogut, and R. F. Klie, *Small* **16**, 1905892 (2020).
- [10] S. Wang *et al.*, *Advanced Functional Materials* **30**, 2004912 (2020).
- [11] F. Raffone, C. Ataca, J. C. Grossman, and G. Cicero, *The Journal of Physical Chemistry Letters* **7**, 2304 (2016).
- [12] P. Yu *et al.*, *Advanced Materials* **29**, 1603991 (2017).
- [13] V. Klee *et al.*, *Nano Letters* **15**, 2612 (2015).
- [14] Q. Gong, S. Sheng, H. Ye, N. Han, L. Cheng, and Y. Li, *Particle & Particle Systems Characterization* **33**, 576 (2016).
- [15] Z. Hemmat *et al.*, *Advanced Materials* **32**, 1907041 (2020).
- [16] J. Cavin *et al.*, *Adv Mater* **33**, e2100347 (2021).
- [17] K. F. Mak, K. L. McGill, J. Park, and P. L. McEuen, *Science* **344**, 1489 (2014).
- [18] D. Voiry, M. Salehi, R. Silva, T. Fujita, M. Chen, T. Asefa, V. B. Shenoy, G. Eda, and M. Chhowalla, *Nano Letters* **13**, 6222 (2013).
- [19] Y. Deng *et al.*, *ACS Nano* **15**, 11526 (2021).

- [20] A. Zunger, MRS Bulletin **22**, 20 (1997).
- [21] S. Wei, L. G. Ferreira, and A. Zunger, Phys Rev B Condens Matter **41**, 8240 (1990).
- [22] L. G. Ferreira, S. H. Wei, and A. Zunger, Phys Rev B Condens Matter **40**, 3197 (1989).
- [23] J. Kang, S. Tongay, J. Li, and J. Wu, J. Appl. Phys. **113**, 143703 (2013).
- [24] J. Kang, S. Tongay, J. Zhou, J. Li, and J. Wu, Applied Physics Letters **102**, 012111 (2013).
- [25] S. M. Oliver *et al.*, 2d Mater **4** (2017).
- [26] Z. Wang *et al.*, Applied Surface Science **504** (2020).
- [27] S. M. Oliver, J. Young, S. Krylyuk, T. L. Reinecke, A. V. Davydov, and P. M. Vora, Communications Physics **3** (2020).
- [28] Y. Li, K. A. Duerloo, K. Wauson, and E. J. Reed, Nat Commun **7**, 10671 (2016).
- [29] O. B. Aslan *et al.*, Nano Lett **18**, 2485 (2018).
- [30] D. Rhodes *et al.*, Nano Lett **17**, 1616 (2017).
- [31] K.-A. N. Duerloo and E. J. Reed, ACS Nano **10**, 289 (2016).
- [32] A. v. d. Walle and M. Asta, Modell. Simul. Mater. Sci. Eng. **10**, 521 (2002).
- [33] M. Sluiter, D. de Fontaine, X. Q. Guo, R. Podloucky, and A. J. Freeman, Physical Review B **42**, 10460 (1990).
- [34] A. van de Walle, M. Asta, and G. Ceder, Calphad **26**, 539 (2002).
- [35] A. M. Holder *et al.*, Science Advances **3** (2017).
- [36] A. Zunger, S. H. Wei, L. G. Ferreira, and J. E. Bernard, Physical Review Letters **65**, 353 (1990).
- [37] S. Wei, L. G. Ferreira, J. E. Bernard, and A. Zunger, Phys Rev B Condens Matter **42**, 9622 (1990).
- [38] A. Zunger, S. Wei, L. G. Ferreira, and J. E. Bernard, Phys Rev Lett **65**, 353 (1990).
- [39] G. Kresse and J. Furthmüller, Computational Materials Science **6**, 15 (1996).
- [40] J. P. Perdew, K. Burke, and M. Ernzerhof, Physical Review Letters **77**, 3865 (1996).
- [41] H. J. Monkhorst and J. D. Pack, Physical Review B **13**, 5188 (1976).

- [42] E. Revolinsky and D. J. Beerntsen, *Journal of Physics and Chemistry of Solids* **27**, 523 (1966).
- [43] K.-A. N. Duerloo, Y. Li, and E. J. Reed, *Nature Communications* **5**, 4214 (2014).
- [44] See Supplemental Material at <http://link.aps.org/supplemental/DOI> for derivations of the mixing enthalpy of alloys with regular and sub-regular solution models.
- [45] S. K. Nemani *et al.*, *ACS Nano* **15**, 12815 (2021).